

PAPER • OPEN ACCESS

# Tailoring the oxygen concentration in Ge-Sb-O alloys to enable femtojoule-level phase-change memory operations




To cite this article: Jiang-Jing Wang *et al* 2022 *Mater. Futures* 1 045302

View the [article online](#) for updates and enhancements.

## You may also like

- [Automatic Satellite Identification in Digital Images](#)  
Jack Smith
- [Light Curve Analysis of Nine Algol \(EA\) Eclipsing Binaries Discovered During the Dauban Survey-additional Data](#)  
David H. Hinz
- [A new laterally conductive bridge random access memory by fully CMOS logic compatible process](#)  
Min-Che Hsieh, Yung-Wen Chin, Yu-Cheng Lin *et al.*

# Tailoring the oxygen concentration in Ge-Sb-O alloys to enable femtojoule-level phase-change memory operations

Jiang-Jing Wang<sup>1,3</sup> , Xiaozhe Wang<sup>1,3</sup>, Yudong Cheng<sup>1</sup>, Jieling Tan<sup>1</sup>, Chao Nie<sup>1</sup>, Zhe Yang<sup>2</sup>, Ming Xu<sup>2</sup> , Xiangshui Miao<sup>2</sup>, Wei Zhang<sup>1,\*</sup>  and En Ma<sup>1</sup>

<sup>1</sup> Center for Alloy Innovation and Design (CAID), State Key Laboratory for Mechanical Behavior of Materials, Xi'an Jiaotong University, Xi'an 710049, People's Republic of China

<sup>2</sup> School of Integrated Circuits, Huazhong University of Science and Technology, Wuhan 430074, People's Republic of China

E-mail: [wzhang0@mail.xjtu.edu.cn](mailto:wzhang0@mail.xjtu.edu.cn)

Received 7 October 2022, revised 3 November 2022

Accepted for publication 4 November 2022

Published 17 November 2022



CrossMark

## Abstract

Chalcogenide phase-change materials (PCMs), in particular, the flagship  $\text{Ge}_2\text{Sb}_2\text{Te}_5$  (GST), are leading candidates for advanced memory applications. Yet, GST in conventional devices suffer from high power consumption, because the RESET operation requires melting of the crystalline GST phase. Recently, we have developed a conductive-bridge scheme for low-power phase-change application utilizing a self-decomposed Ge-Sb-O (GSO) alloy. In this work, we present thorough structural and electrical characterizations of GSO thin films by tailoring the concentration of oxygen in the phase-separating GSO system. We elucidate a two-step process in the as-deposited amorphous film upon the introduction of oxygen: with increasing oxygen doping level, germanium oxides form first, followed by antimony oxides. To enable the conductive-bridge switching mode for femtojoule-level RESET energy, the oxygen content should be sufficiently low to keep the antimony-rich domains easily crystallized under external electrical stimulus. Our work serves as a useful example to exploit alloy decomposition that develops heterogeneous PCMs, minimizing the active switching volume for low-power electronics.

Keywords: phase-change memory, amorphous phase, low-power, conductive-bridge, decomposition

<sup>3</sup> These authors made equal contribution.

\* Author to whom any correspondence should be addressed.



Original content from this work may be used under the terms of the [Creative Commons Attribution 4.0 licence](https://creativecommons.org/licenses/by/4.0/). Any further distribution of this work must maintain attribution to the author(s) and the title of the work, journal citation and DOI.

### Future perspectives

The rapidly growing demand for data storage and processing is posing a serious challenge for the current computing architecture. Emerging non-volatile memory combines the advantages of both fast operation and persistent storage, holding great promises to improve the computing and energy efficiencies by substantially reducing the heavy data traffic between multiple electronic units. Among the competing materials candidates, phase-change materials (PCMs) that exploit phase transitions between the crystalline and amorphous states are at the forefront for commercialization. Despite the success of PCMs in high-density binary storage, e.g. the 3D Xpoint memory products, much efforts are being taken to further improve the materials properties to enable devices with lower power consumption, faster switching speed, better thermal stability, wider contrast window as well as suppressed resistance drift. The design and synthesis of new materials that can achieve these goals are critical for the development of phase-change memory devices for multilevel storage, neuro-inspired computing, photonic computing, and flexible displays.

## 1. Introduction

The total data volume worldwide has been drastically increased in the past decades, and is predicted to reach  $10^{23}$  bytes by 2025. Storing and processing the massive datasets quickly and accurately at a manageable energy cost poses a serious challenge for current electronic devices. The emerging non-volatile memory [1–3] and neuro-inspired computing [4–6] technologies hold great promises to cope with this data crisis. Such novel electronic or optoelectronic devices rely on the development of new materials, such as phase-change materials (PCMs) [7–13], resistive-switching oxides [14], ferroelectric [15] and spintronic materials [16], two-dimensional materials [17] and polymers [18]. Among these promising materials candidates, PCMs are already technologically mature, and have been commercialized recently [19]. The basic working principle is to utilize the rapid switching capability of PCM, in particular,  $\text{Ge}_2\text{Sb}_2\text{Te}_5$  (GST), between its crystalline state and amorphous phase for memory programming [7–12]. The logic states ‘0’ and ‘1’ are defined by the large contrast in electrical resistance [20–23] or optical reflectance/transmission [24–28] of the two solid states, which originate from a fundamental change in electronic structure and bonding character upon phase transition [29–32].

The crystallization (SET) or amorphization (RESET) of GST proceeds via Joule heating brought by external pulses. To amorphize the crystalline state, the rigid lattice needs to be melted down first. This step is the bottleneck in terms of energy cost, because of the high melting temperature of GST ( $\sim 900$  K). Device miniaturization with proper thermal insulations is typically used to reduce power consumption [33]. But conventional GST devices still require tens of picojoules to nanojoules for each RESET operation. In 2011, Xiong *et al* managed to deposit GST into the nanogaps between carbon nanotubes (serving as electrodes), which drastically reduced the switching volume, leading to  $\sim 100$  femtojoules per

RESET operation [34]. Further optimization was made by using GST nanowires and carbon nanotubes electrodes in 2013, reaching a RESET energy of  $\sim 80$  femtojoules [35]. In 2022, Wang *et al* have developed a more realistic approach to reduce the active switching volume of GST for integrated devices with an ultrascaled edge-electrode using very narrow graphene nanoribbons embedded in hexagonal boron nitride multilayer, reaching  $\sim 54$  femtojoules per RESET operation [36].

In parallel to these device miniaturization schemes, much progress has also been made in designing new materials to achieve low-power operations while keeping the device structure unchanged. By alloying  $\text{Sb}_2\text{Te}_3$ , the parent phase of GST, with various transition metal dopants, such as scandium [37–45], yttrium [46–50], titanium [51–54] and others [55–57], the RESET energy can be reduced by approximately one order of magnitude as compared to GST in the same device condition. This could be generally attributed to the easier disordering (melting) of the rocksalt-like lattice with higher concentration of atomic vacancies [37]. Another effective approach is to replace the homogeneous switching medium with the  $\text{GeTe}/\text{Sb}_2\text{Te}_3$  superlattice [58–65] or the  $\text{TiTe}_2/\text{Sb}_2\text{Te}_3$  heterostructure [66–71]. The working mechanism of the former is still under debate, while the latter features a quasi-two-dimensional switching of  $\text{Sb}_2\text{Te}_3$  under confinement of robust  $\text{TiTe}_2$  crystalline nanolayers. The melting of only the  $\text{Sb}_2\text{Te}_3$  nanolayers and the high thermal barrier brought by the  $\text{TiTe}_2$  walls also result in about one order of magnitude reduction in RESET energy [66]. Sub-picojoule amorphization energy was also reported by using a  $\text{Cr}_2\text{Ge}_2\text{Te}_6$  layered material [72].

In early 2022, we have designed a conductive-bridge phase-change memory (cbPCM) scheme [73] that combines the advantages of phase-change memory with filamentary-switching in metal oxides. The essential idea is to minimize the active switching volume in conventional devices via phase separation. Under external stimulus, e.g. heating or electrical pulses, the switching medium spontaneously decomposes into a heterogeneous network with domains having different crystallization temperature,  $T_x$ . As sketched in figure 1(a), a conductive path forms in the amorphous matrix (high  $T_x$ ) by crystallizing only the nanobridges between different crystalline nanodomains (low  $T_x$ ). In [73], we chose to incorporate oxygen into Ge-Sb alloys [74–76] to increase their tendency to self-decompose into Ge-enriched and Sb-enriched regions intermingled in a network, and have achieved an average RESET energy of  $\sim 43$  femtojoules per operation using a set of Ge-Sb-O (GSO) devices. The essential ingredient that makes functional GSO devices is the oxygen content in the alloy, which however requires very careful control and calibration. In this work, we monitor the degree of oxidation during the alloy film deposition process and show that the concentration of oxygen has to be maintained at a relatively low level; otherwise, inside a heavily oxidized amorphous matrix it would no longer be feasible to create a conductive path.

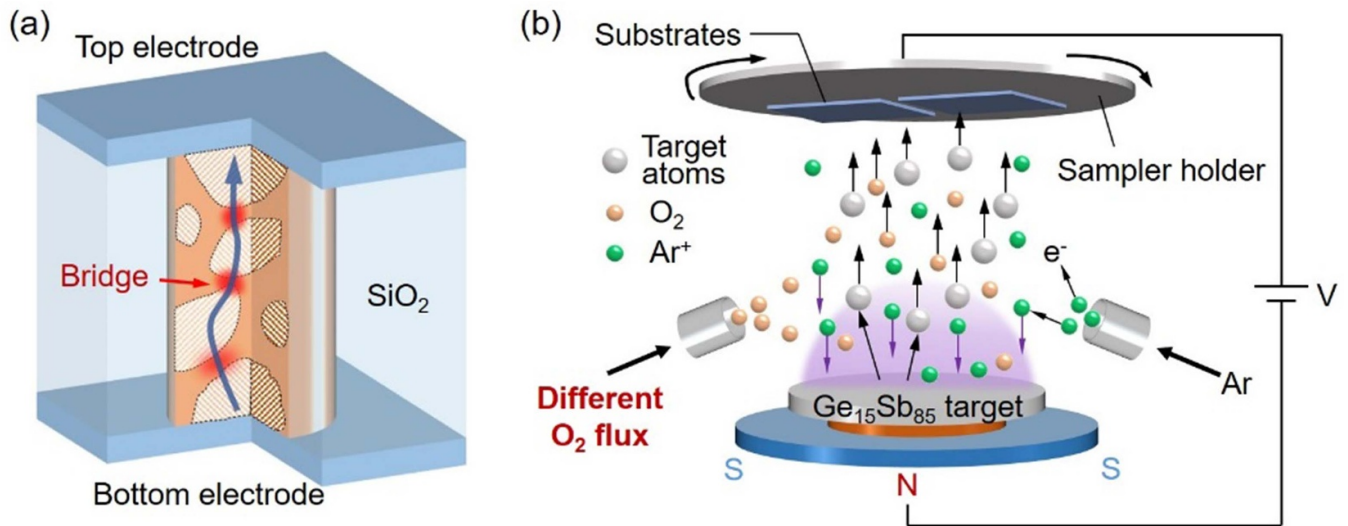


**Figure 1.** Tailoring the degree of oxygen incorporation in Ge-Sb-O alloys. (a) The sketch of a potential conductive path inside the heterogeneous network consisting of Sb-rich crystalline nanodomains and Sb-poor glass matrix. (b) Schematic depicting the sputtering of a  $\text{Ge}_{15}\text{Sb}_{85}$  alloy target with varied  $\text{O}_2$  flux under a protective atmosphere (Argon), resulting in oxygen incorporation to various levels.

## 2. Results and discussion

We deposited various GSO thin films of  $\sim 100$  nm thickness using a high-purity  $\text{Ge}_{15}\text{Sb}_{85}$  alloy target under  $\text{O}_2$  flow on silicon/silica substrate through direct current magnetron sputtering at room temperature, as sketched in figure 1(b). The sputtering power was set as 30 W and deposition rate was calibrated as  $\sim 100$  nm  $\text{min}^{-1}$ . The  $\text{O}_2$  flow rate was adjusted from 0 to 12.5 sccm under protective Ar flow of 50 sccm. The pressure of the chamber was 0.5 Pa. A  $\sim 5$  nm ZnS- $\text{SiO}_2$  capping layer was also deposited to prevent further oxidation at the surface. The five GSO thin films under  $\text{O}_2$  flow rate = 0, 2, 5, 7.5 and 12.5 sccm were then used for electrical resistance, x-ray diffraction (XRD) pattern, Raman spectroscopy and x-ray photoelectron spectroscopy (XPS) and energy-dispersive spectroscopy (EDS) measurements.

The temperature-dependent electrical resistance ( $R$ - $T$ ) measurements were made using the van der Pauw method. Figure 2(a) shows the change in sheet resistance of the five thin films upon heating with a heating rate of  $10$   $^{\circ}\text{C min}^{-1}$ . With moderate oxygen doping below 7.5 sccm, the GSO thin films show a similar  $R$ - $T$  profile as compared to the undoped  $\text{Ge}_{15}\text{Sb}_{85}$  thin film [77–79] with a clear drop at  $T_x \sim 235$   $^{\circ}\text{C}$ , indicating the onset of crystallization. Yet, a gradual increase in resistance is observed for both the initial amorphous phase and the annealed phase at  $300$   $^{\circ}\text{C}$  as the oxygen concentration increases. A clear deviation in the  $R$ - $T$  profile is observed in the heavily doped GSO thin film (12.5 sccm), which shows a higher  $T_x \sim 260$   $^{\circ}\text{C}$  and a much larger sheet resistance value at  $300$   $^{\circ}\text{C}$  as compared to the other four thin films.

To assess the structural properties of the thin films after heating, we carried out XRD measurements at room temperature. As displayed in figure 2(b), the undoped  $\text{Ge}_{15}\text{Sb}_{85}$  thin

film shows major reflections at (003), (101), (006) and (202), corresponding to the rhombohedral phase of Sb-rich domains [79]. The four GSO thin films also crystallized in the rhombohedral phase with Sb-rich grains, despite the change in crystallographic orientation, showing major reflections at (012) and (110). The (012) peak is gradually broadened as the oxygen level increases, indicating increased structural disorder upon the introduction of oxygen. No sign of pure Ge nor  $\text{GeO}_2$  crystallites was observed in the annealed GSO thin films.

Figure 2(c) shows the Raman spectroscopy measurements (using an excitation laser wavelength of 532 nm) of the annealed thin films in the range of  $100$ – $250$   $\text{cm}^{-1}$ . In the undoped case, the peaks in  $115$   $\text{cm}^{-1}$  and  $155$   $\text{cm}^{-1}$  correspond to the  $E_g$  and  $A_{1g}$  modes of rhombohedral Sb [80]. The two peaks merged gradually with the increase of oxygen alloying. To understand this behavior, we used two Lorentzian functions to fit the spectra between  $100$   $\text{cm}^{-1}$  and  $175$   $\text{cm}^{-1}$  and evaluate the full-width half maximum (FWHM) values and peak positions of the two modes. The sum of fitted curve is marked by red dash-dot line, the fitted  $E_g$  and  $A_{1g}$  modes are indicated by green and blue lines, respectively. The corresponding FWHM values and peak positions are given in figure 2(d), which shows that oxygen doping induces a pronounced broadening of the  $E_g$  mode with FWHM increasing from  $14$   $\text{cm}^{-1}$ – $29$   $\text{cm}^{-1}$ , and also a slight broadening of the  $A_{1g}$  mode. In addition, opposite shift in the peak position is found in the  $E_g$  mode (blue shift) and the  $A_{1g}$  mode (red shift), leading to a progressive merging of the two peaks.

In general, crystalline phase of high uniformity in terms of bond angles and lengths results in a limited number of vibration states, and hence sharp Raman peaks at characteristic wavenumbers. In contrast, amorphous phase with disordered

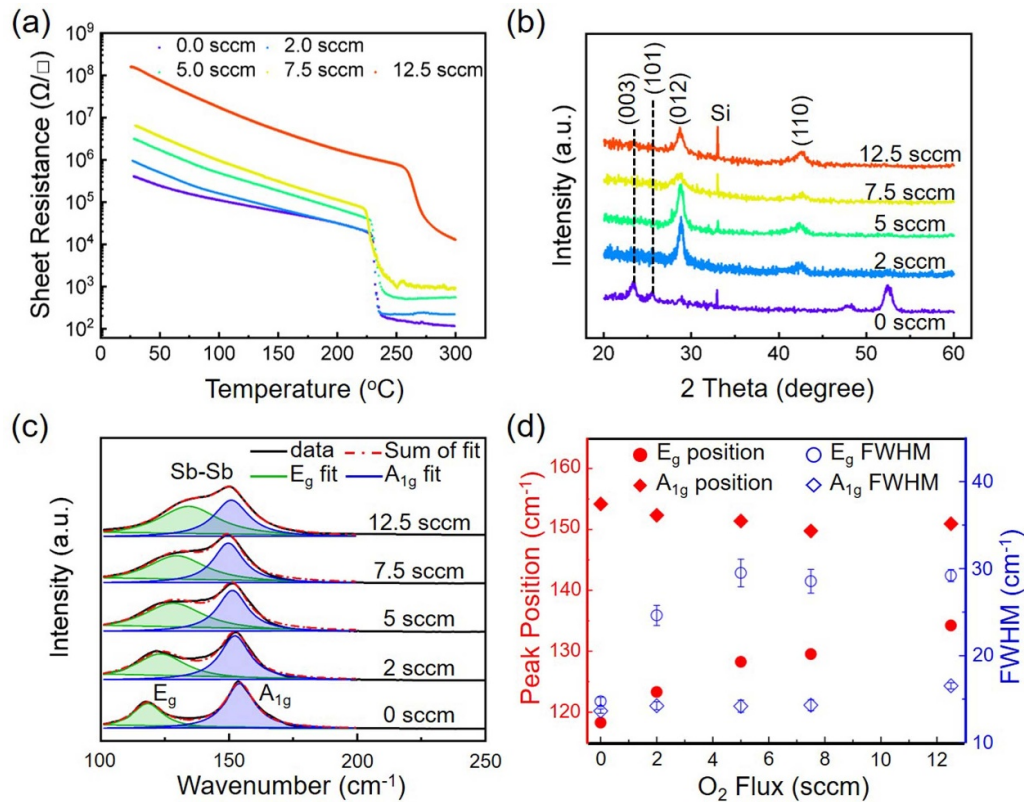


**Figure 2.** Electrical and structural characterizations of GSO thin films. (a) The resistance-temperature ( $R$ - $T$ ) curves of Ge<sub>15</sub>Sb<sub>85</sub> and four GSO thin films upon heating. (b) The room temperature XRD pattern measurements of the five annealed thin films obtained after  $R$ - $T$  measurements done at 300 °C. (c) The Raman spectra of the annealed thin films in the range of 100 and 250 cm<sup>-1</sup>. The fitted E<sub>g</sub> and A<sub>1g</sub> modes are marked in green and blue, respectively. (d) The corresponding peak positions and FWHM values.

atomic arrangement exhibits a much wider range of bond angles and bond lengths, and the distribution of possible states leads to broader Raman peaks [81–84]. In our measurements, the enlarged FWHM values of the E<sub>g</sub> and A<sub>1g</sub> mode indicate an incomplete crystallization with oxygen doping, despite thermal annealing at relatively high temperatures. This behavior can be attributed to the much higher crystallization temperatures of oxides, e.g. the GeO<sub>2</sub> glass has a  $T_x$  above 700 °C [85].

To gain a better understanding of the amorphous phase, we carried out XPS measurements on the as-deposited thin films. All binding energies were corrected with respect to the C 1 s peak. Figure 3(a) shows the Ge 2p spectra with the binding energy range between 1210–1225 eV. In undoped Ge<sub>15</sub>Sb<sub>85</sub>, the peak of Ge 2p<sub>3/2</sub> is detected at ~1218 eV, corresponding to the Ge homopolar bonds (Ge–Ge) [86]. Even with a relatively low doping level of oxygen (2 sccm), the Ge–Ge peak is already weakened, and a distinct peak of Ge–O at ~1220 eV is identified. As the oxygen doping increases to 5 sccm, the Ge–Ge peak is no longer visible, leaving only the GeO<sub>2</sub> peak. Figure 3(b) shows the Sb 3d spectra between 525–545 eV. The Sb 3d spectrum of undoped Ge<sub>15</sub>Sb<sub>85</sub> exhibits two contributions, 3d<sub>5/2</sub> and 3d<sub>3/2</sub>, due to the spin-orbit splitting, which are located at ~528 eV and ~538 eV, respectively. Small Sb–O contributions start to appear at ~531 eV and ~540 eV in the

GSO thin film obtained under 5 sccm oxygen flux, stemming from the formation of Sb<sub>2</sub>O<sub>3</sub> [87]. The two peaks are further enhanced as oxygen doping level increases.

This two-step oxidation process can be explained by the stronger tendency to form germanium oxides, as their formation energy is much more favorable than that of antimony oxides [73]. Unlike germanium, antimony is the main component of the thin film, hence the Sb–Sb peaks still remain high even in the heavily doped GSO thin film (12.5 sccm). But if the major fraction of antimony is also oxidized, no sign of crystallization can be observed below 300 °C [76]. To design readily switchable conductive bridges, we need to keep a low  $T_x$  for the Sb-rich domains so that they can be easily crystallized with external thermal or electrical stimulus. Therefore, excessive oxygen content in antimony should be prevented. From the above analyses, we regard 2–5 sccm as the suitable oxygen flow rate range for sputtering Ge<sub>15</sub>Sb<sub>85</sub>, and such flow rates should be further reduced if a Sb-richer alloy target is used. With high oxygen flow rate (12.5 sccm), the oxygen concentration in these GSO thin films was estimated to exceed 35 at% by EDS measurements, while less oxygen was incorporated into the thin films in the range of 10–16 at% at 2–5 sccm. The latter is compatible with that reported in [73], ~16 at%, which was determined by atom-probe tomography measurements.



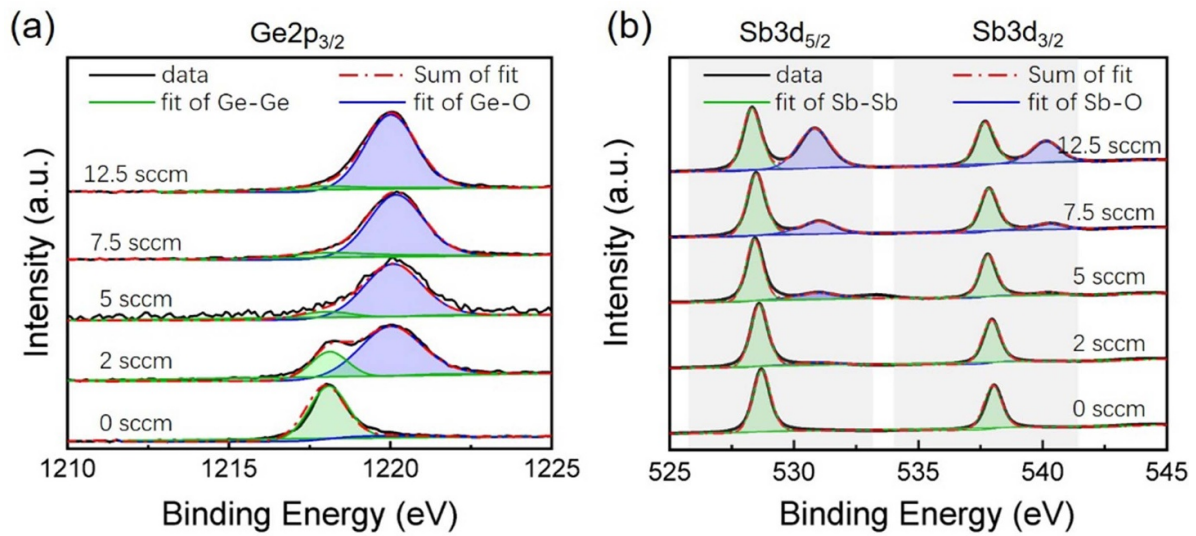


**Figure 3.** High-resolution XPS spectra of (a) Ge 2p<sub>3/2</sub> and (b) Sb 3d for as-deposited Ge<sub>15</sub>Sb<sub>85</sub> thin films prepared under different oxygen flux. The blue and green regions represent the fitting of different components, and the sum of fitted curves are marked by red dash-dot line.

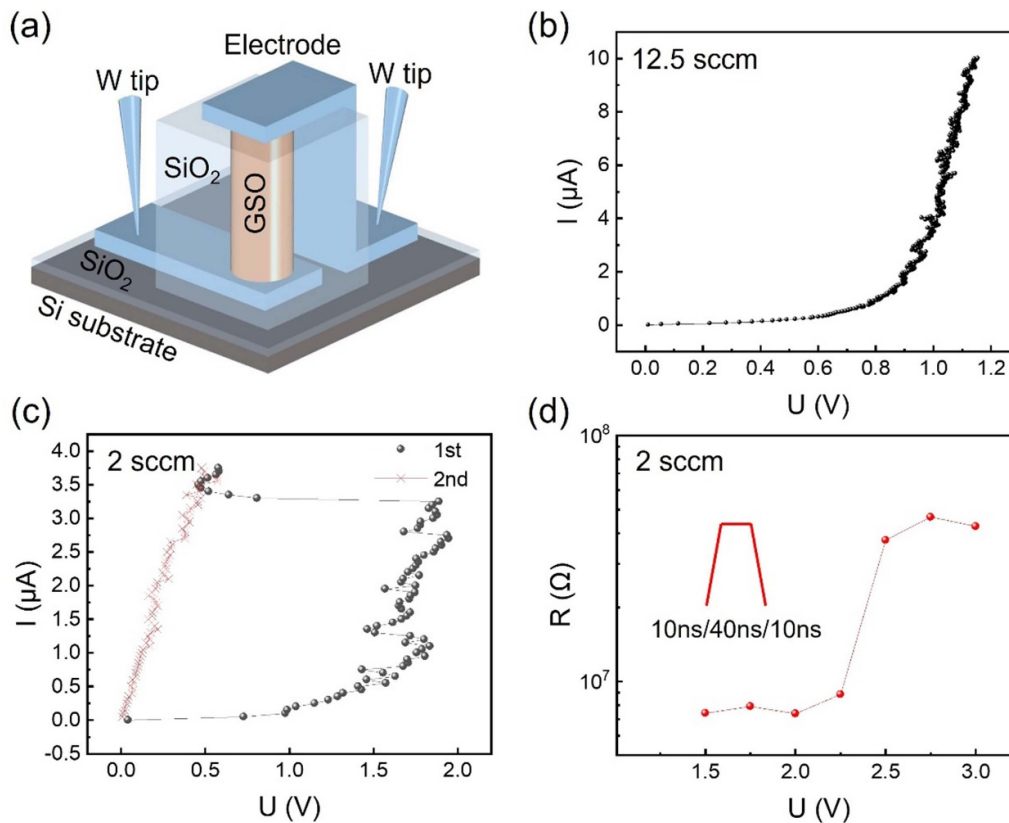


**Figure 4.** Electrical performance of the GSO devices. (a) Schematic of the experimental setup for electrical testing of GSO devices in a probe station. (b) and (c) The current–voltage ( $I$ – $V$ ) characteristics of the GSO devices with heavy and light oxygen doping by DC sweeps. (d) The resistance–voltage ( $R$ – $V$ ) characteristics of the 2 sccm GSO device under RESET operation. The applied pulse waveform is shown in the inset.

For validation, we fabricated two GSO devices with light and heavy oxygen doping. Figure 4(a) shows the device structure. A hole with diameter of  $\sim 250$  nm was etched in a  $\sim 100$  nm thick SiO<sub>2</sub> dielectric layer, and the Ge<sub>15</sub>Sb<sub>85</sub> target was sputtered under oxygen flow rate of 2 and 12.5 sccm

for the two devices. The devices were covered with a  $\sim 50$  nm tungsten electrode thin layer to prevent further oxidation. Then we applied DC sweeps to the two devices to pattern the heterogeneous network. As seen in the current–voltage ( $I$ – $V$ ) profiles, the heavily O-doped GSO device showed a highly

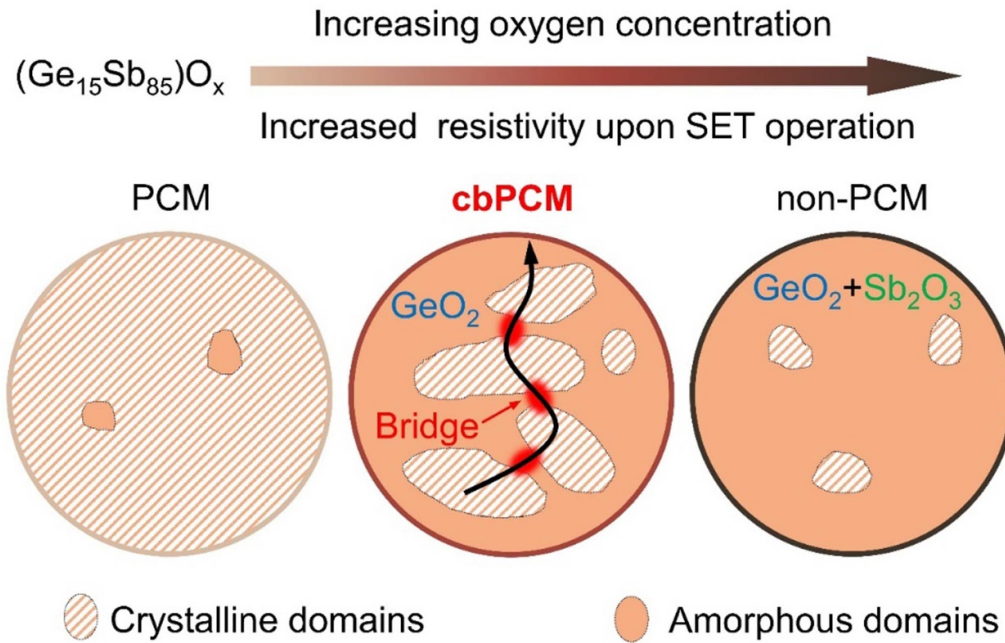


**Figure 5.** The sketch of different working modes as the oxygen concentration in GSO alloys increases. Upon SET operation, the ratio of crystalline/amorphous domains varies significantly as a function of oxygen concentration.

resistive behavior up to  $10 \mu\text{A}$  (figure 4(b)), while the other device was switched to a low-resistance state at  $\sim 3.25 \mu\text{A}$ , and the subsequent DC sweep confirmed the conductive nature of the latter device (figure 4(c)). The former device is regarded as a RESET-stuck failure, due to over-oxidation. Figure 4(d) shows a typical RESET operation of GSO device with suitable oxygen doping. To guarantee a low RESET energy  $E_{\text{RESET}} = I \times U \times \Delta t = U_{\text{RESET}}^2 \times \Delta t / R_{\text{SET}}$ , it is desirable to have a SET state with relatively high resistance [73], e.g.  $7.5 \text{ M}\Omega$  in this case. By applying a series of voltage pulses with  $\Delta t = 50 \text{ ns}$  (FWHM), the resistance of the device increased to more than  $40 \text{ M}\Omega$  at  $\sim 2.5 \text{ V}$ . The RESET energy is estimated as  $\sim 41.6 \text{ fJ}$ , close to the average value reported in [73].

Figure 5 summarizes how to enable the cbPCM working mode via oxidation. With low-level oxygen incorporation, amorphous GSO alloys get crystallized almost completely upon SET operation. The potential presence of amorphous domains due to oxidation can hardly alter the electrical performance of GSO devices, as the electric current can pass through the crystalline matrix easily. The switching of GSO proceeds in the conventional PCM mode. Regarding the heavily oxidized case, the vast majority of germanium and antimony atoms form strong bonds with oxygen atoms. The high crystallization temperature of  $\text{GeO}_2$  and  $\text{Sb}_2\text{O}_3$  makes the glass domains insensitive to SET pulses. Therefore, GSO devices get stuck in the high-resistance state, and cannot be programmed. Only with moderate-level oxygen incorporation, GSO devices can function in the cbPCM mode with robust  $\text{GeO}_2$ -dominant glass domains and Sb-rich crystalline domains so that the nanobridges in between can be effectively switched. To achieve this goal, the formation of antimony oxides in large fractions must be avoided, and it is important to use an alloy target with relatively high

germanium concentration, such as  $\text{Ge}_{15}\text{Sb}_{85}$ , for sputtering to guarantee the abundance of germanium oxides glass in the heterogeneous network.

### 3. Conclusions

In summary, we have reported a thorough experimental characterization of the self-decomposed GSO alloys for low-power phase-change memory application. We have tailored the oxygen concentration in the  $\text{Ge}_{15}\text{Sb}_{85}$  thin films and revealed a two-step oxidation process as the doping level gradually increased. We note that the relatively rich germanium concentration and moderate oxygen doping are essential to build the heterogeneous network with an intermixed  $\text{GeO}_2$  glass domains and Sb-rich crystalline domains, allowing the formation of conductive path under external electrical stimulus. This spontaneous decomposition in the GSO alloy reduces the active switching volume sharply despite large contact areas with electrodes, as only parts of the conductive bridge need to be melted upon RESET pulsing. We note that this cbPCM scheme inevitably introduces certain randomness for device programming, as the formation of heterogeneous network differs from device to device. In addition to binary storage, heterogeneous PCMs could also be useful for the emulation of stochastic phase-change neurons [88] and for the development of physical unclonable functions [89].

### Acknowledgments

The authors thank Miss Dan He and Miss Chenyu Liang at Instrument Analysis Center of Xi'an Jiaotong University for their assistance with Raman and XPS measurements. E M

acknowledges the National Natural Science Foundation of China (Grant No. 52150710545). The authors acknowledge the 111 project 2.0 (BP2018008) and the International Joint Laboratory for Micro/Nano Manufacturing and Measurement Technologies of XJTU. W Z and E M also acknowledge the support of XJTU for their work at CAID. X M acknowledges the National Natural Science Foundation of China (Grant No. 62174060) and the funding for Hubei Key Laboratory of Advanced Memories.

## Conflict of interest

The authors declare no competing interests

## ORCID iDs

Jiang-Jing Wang  <https://orcid.org/0000-0001-7327-8159>

Ming Xu  <https://orcid.org/0000-0002-2730-283X>

Wei Zhang  <https://orcid.org/0000-0002-0720-4781>

## References

- [1] Wong H-S P and Salahuddin S 2015 Memory leads the way to better computing *Nat. Nanotechnol.* **10** 191–4
- [2] Zhang Z, Wang Z, Shi T, Bi C, Rao F, Cai Y, Liu Q, Wu H and Zhou P 2020 Memory materials and devices: from concept to application *InfoMat.* **2** 261–90
- [3] Wang Z, Wu H, Burr G W, Hwang C S, Wang K L, Xia Q and Yang J J 2020 Resistive switching materials for information processing *Nat. Rev. Mater.* **5** 173–95
- [4] Zidan M A, Strachan J P and Lu W D 2018 The future of electronics based on memristive systems *Nat. Electron.* **1** 22–29
- [5] Sebastian A, Le Gallo M, Khaddam-Aljameh R and Eleftheriou E 2020 Memory devices and applications for in-memory computing *Nat. Nanotechnol.* **15** 529–44
- [6] Zhang Y et al 2020 Brain-inspired computing with memristors: challenges in devices, circuits, and systems *Appl. Phys. Rev.* **7** 011308
- [7] Wuttig M and Yamada N 2007 Phase-change materials for rewriteable data storage *Nat. Mater.* **6** 824–32
- [8] Zhang W, Mazzarello R, Wuttig M and Ma E 2019 Designing crystallization in phase-change materials for universal memory and neuro-inspired computing *Nat. Rev. Mater.* **4** 150–68
- [9] Sebastian A, Le Gallo M, Burr G W, Kim S, BrightSky M and Eleftheriou E 2018 Tutorial: brain-inspired computing using phase-change memory devices *J. Appl. Phys.* **124** 111101
- [10] Wong H-S P, Raoux S, Kim S, Liang J, Reifenberg J P, Rajendran B, Asheghi M and Goodson K E 2010 Phase change memory *Proc. IEEE* **98** 2201
- [11] Song Z, Song S, Zhu M, Wu L, Ren K, Song W and Feng S 2018 From octahedral structure motif to sub-nanosecond phase transitions in phase change materials for data storage *Sci. China Inf. Sci.* **61** 081302
- [12] Xu M, Mai X, Lin J, Zhang W, Li Y, He Y, Tong H, Hou X, Zhou P and Miao X 2020 Recent advances on neuromorphic devices based on chalcogenide phase-change materials *Adv. Funct. Mater.* **30** 2003419
- [13] Xu M, Xu M and Miao X 2022 Deep machine learning unravels the structural origin of mid-gap states in chalcogenide glass for high-density memory integration *InfoMat.* **4** e12315
- [14] Pan F, Gao S, Chen C, Song C and Zeng F 2014 Recent progress in resistive random access memories: materials, switching mechanisms, and performance *Mater. Sci. Eng. R* **83** 1–59
- [15] Scott J F and de Araujo C A P 1989 Ferroelectric memories *Science* **246** 1400–5
- [16] Kent A D and Worledge D C 2015 A new spin on magnetic memories *Nat Nanotechnol.* **10** 187–91
- [17] Liu L, Sun Y, Huang X, Liu C, Tang Z, Zeng S, Zhang D W, Deng S and Zhou P 2022 Ultrafast flash memory with large self-rectifying ratio based on atomically thin MoS<sub>2</sub>-channel transistor *Mater. Futures* **1** 025301
- [18] Ouyang J, Chu C-W, Szmanda C R, Ma L and Yang Y 2004 Programmable polymer thin film and non-volatile memory device *Nat. Mater.* **3** 918–22
- [19] Yoon K J, Kim Y and Hwang C S 2019 What will come after V-NAND—vertical resistive switching memory? *Adv. Electron. Mater.* **5** 1800914
- [20] Ovshinsky S 1968 Reversible electrical switching phenomena in disordered structures *Phys. Rev. Lett.* **21** 1450–3
- [21] Redaelli A, Pirovano A, Pellizzer F, Lacaíta A L, Ielmini D and Bez R 2004 Electronic switching effect and phase change transition in chalcogenide materials *IEEE Electron. Dev. Lett.* **25** 684
- [22] Siegrist T, Jost P, Volker H, Woda M, Merkelbach P, Schlockermann C and Wuttig M 2011 Disorder-induced localization in crystalline phase-change materials *Nat. Mater.* **10** 202–8
- [23] Zhang W, Thiess A, Zalden P, Zeller R, Dederichs P H, Raty J-Y, Wuttig M, Blügel S and Mazzarello R 2012 Role of vacancies in metal-insulator transitions of crystalline phase-change materials *Nat. Mater.* **11** 952–6
- [24] Yamada N, Ohno E, Nishiuchi K, Akahira N and Takao M 1991 Rapid-phase transitions of GeTe-Sb<sub>2</sub>Te<sub>3</sub> pseudobinary amorphous thin films for an optical disk memory *J. Appl. Phys.* **69** 2849–56
- [25] Shportko K, Kremers S, Woda M, Lencer D, Robertson J and Wuttig M 2008 Resonant bonding in crystalline phase-change materials *Nat. Mater.* **7** 653–8
- [26] Huang B and Robertson J 2010 Bonding origin of optical contrast in phase-change memory materials *Phys. Rev. B* **81** 081204(R)
- [27] Hosseini P, Wright C D and Bhaskaran H 2014 An optoelectronic framework enabled by low-dimensional phase-change films *Nature* **511** 206–11
- [28] Feldmann J et al 2021 Parallel convolutional processing using an integrated photonic tensor core *Nature* **589** 52–58
- [29] Zhang W, Mazzarello R and Ma E 2019 Phase-change materials in electronics and photonics *MRS Bull.* **44** 686–90
- [30] Raty J Y, Schumacher M, Golub P, Deringer V L, Gatti C and Wuttig M 2019 A quantum-mechanical map for bonding and properties in solids *Adv. Mater.* **31** 1806280
- [31] Zhang W and Ma E 2020 Unveiling the structural origin to control resistance drift in phase-change memory materials *Mater. Today* **41** 156–76
- [32] Lee T H and Elliott S R 2022 Hypervalency in amorphous chalcogenides *Nat. Commun.* **13** 1458
- [33] Fong S W, Neumann C M and Wong H-S P 2017 Phase-change memory—towards a storage-class memory *IEEE Trans. Electron. Dev.* **64** 4374–85
- [34] Xiong F, Liao A D, Estrada D and Pop E 2011 Low-power switching of phase-change materials with carbon nanotube electrodes *Science* **332** 568–70
- [35] Xiong F, Bae M-H, Dai Y, Liao A D, Behnam A, Carrion E A, Hong S, Ielmini D and Pop E 2013 Self-aligned



- nanotube-nanowire phase change memory *Nano Lett.* **13** 464–9
- [36] Wang X et al 2022 Minimizing the programming power of phase change memory by using graphene nanoribbon edge-contact *Adv. Sci.* **9** e2202222
- [37] Rao F et al 2017 Reducing the stochasticity of crystal nucleation to enable subnanosecond memory writing *Science* **358** 1423–7
- [38] Akola J and Jones R O 2017 Speeding up crystallization *Science* **358** 1386
- [39] Zewdie G M, Zhou Y-X, Sun L, Rao F, Deringer V L, Mazzarello R and Zhang W 2019 Chemical design principles for cache-type Sc-Sb-Te phase-change memory materials *Chem. Mater.* **31** 4008–15
- [40] Ding K, Chen B, Chen Y, Wang J, Shen X and Rao F 2020 Recipe for ultrafast and persistent phase-change memory materials *NPG Asia Mater.* **12** 63
- [41] Chen B et al 2019 Kinetics features conducive to cache-type nonvolatile phase-change memory *Chem. Mater.* **31** 8794–800
- [42] Wang X-P, Li X-B, Chen N-K, Bang J, Nelson R, Ertural C, Dronskowski R, Sun H-B and Zhang S 2020 Time-dependent density-functional theory molecular-dynamics study on amorphization of Sc-Sb-Te alloy under optical excitation *NPJ Comput. Mater.* **6** 31
- [43] Qiao C, Guo Y R, Wang S Y, Xu M, Miao X, Wang C Z and Ho K M 2019 Local structure origin of ultrafast crystallization driven by high-fidelity octahedral clusters in amorphous  $\text{Sc}_0.2\text{Sb}_2\text{Te}_3$  *Appl. Phys. Lett.* **114** 071901
- [44] Hu S, Xiao J, Zhou J, Elliott S R and Sun Z 2020 Synergy effect of co-doping Sc and Y in  $\text{Sb}_2\text{Te}_3$  for phase-change memory *J. Mater. Chem. C* **8** 6672–9
- [45] Hu S, Liu B, Li Z, Zhou J and Sun Z 2019 Identifying optimal dopants for  $\text{Sb}_2\text{Te}_3$  phase-change material by high-throughput *ab initio* calculations with experiments *Comput. Mater. Sci.* **165** 51–58
- [46] Li Z, Si C, Zhou J, Xu H and Sun Z 2016 Yttrium-Doped  $\text{Sb}_2\text{Te}_3$ : a promising material for phase-change Memory *ACS Appl. Mater. Interfaces* **8** 26126–34
- [47] Li Z, Miao N, Zhou J, Xu H and Sun Z 2017 Reduction of thermal conductivity in  $\text{Y}_x\text{Sb}_{2-x}\text{Te}_3$  for phase change memory *J. Appl. Phys.* **122** 195107
- [48] Liu B, Liu W, Li Z, Li K, Wu L, Zhou J, Song Z and Sun Z 2020 Y-Doped  $\text{Sb}_2\text{Te}_3$  phase-change materials: toward a universal memory *ACS Appl. Mater. Interfaces* **12** 20672–9
- [49] Liu B, Li K, Liu W, Zhou J, Wu L, Song Z, Elliott S R and Sun Z 2021 Multi-level phase-change memory with ultralow power consumption and resistance drift *Sci. Bull.* **66** 2217
- [50] Zhou Y, Sun L, Zewdie G M, Mazzarello R, Deringer V L, Ma E and Zhang W 2020 Bonding similarities and differences between Y-Sb-Te and Sc-Sb-Te phase-change memory materials *J. Mater. Chem. C* **8** 3646–54
- [51] Zhu M et al 2014 One order of magnitude faster phase change at reduced power in Ti-Sb-Te *Nat. Commun.* **5** 4086
- [52] Xia M, Zhu M, Wang Y, Song Z, Rao F, Wu L, Cheng Y and Song S 2015 Ti-Sb-Te alloy: a candidate for fast and long-life phase-change memory *ACS Appl. Mater. Interfaces* **7** 7627–34
- [53] Zhu M, Xia M, Song Z, Cheng Y, Wu L, Rao F, Song S, Wang M, Lu Y and Feng S 2015 Understanding the crystallization behavior of as-deposited Ti-Sb-Te alloys through real-time radial distribution functions *Nanoscale* **7** 9935–44
- [54] Rao F, Song Z, Cheng Y, Liu X, Xia M, Li W, Ding K, Feng X, Zhu M and Feng S 2015 Direct observation of titanium-centered octahedra in titanium-antimony-tellurium phase-change material *Nat. Commun.* **6** 10040
- [55] Zheng Y, Qi R, Cheng Y and Song Z 2019 The crystallization mechanism of zirconium-doped  $\text{Sb}_2\text{Te}_3$  material for phase-change random-access memory application *J. Mater. Sci., Mater. Electron.* **31** 5861–5
- [56] Xue Y, Cheng Y, Zheng Y, Yan S, Song W, Lv S, Song S and Song Z 2020 Phase change memory based on Ta-Sb-Te alloy—towards a universal memory *Mater. Today Phys.* **15** 100266
- [57] Zhao J, Song W X, Xin T and Song Z 2021 Rules of hierarchical melt and coordinate bond to design crystallization in doped phase change materials *Nat. Commun.* **12** 6473
- [58] Chong T C, Shi L P, Zhao R, Tan P K, Li J M, Lee H K, Miao X S, Du A Y and Tung C H 2006 Phase change random access memory cell with superlattice-like structure *Appl. Phys. Lett.* **88** 122114
- [59] Simpson R E, Fons P, Kolobov A V, Fukaya T, Krbal M, Yagi T and Tominaga J 2011 Interfacial phase-change memory *Nat. Nanotechnol.* **6** 501–5
- [60] Khan A I, Daus A, Islam R, Neilson K M, Lee H R, Wong H-S P and Pop E 2021 Ultralow-switching current density multilevel phase-change memory on a flexible substrate *Science* **373** 1243–7
- [61] Li X-B, Chen N-K, Wang X-P and Sun H-B 2018 Phase-change superlattice materials toward low power consumption and high density data storage: microscopic picture, working principles, and optimization *Adv. Funct. Mater.* **28** 1803380
- [62] Lotnyk A, Behrens M and Rauschenbach B 2019 Phase change thin films for non-volatile memory applications *Nanoscale Adv.* **1** 3836–57
- [63] Momand J, Wang R, Boschker J E, Verheijen M A, Calarco R and Kooi B J 2015 Interface formation of two- and three-dimensionally bonded materials in the case of GeTe-Sb<sub>2</sub>Te<sub>3</sub> superlattices *Nanoscale* **7** 19136–43
- [64] Boniardi M, Boschker J E, Momand J, Kooi B J, Redaelli A and Calarco R 2019 Evidence for thermal-based transition in Super-lattice (SL) phase change memory *Phys. Status Solidi RRL* **13** 1800634
- [65] Térébéné D, Castellani N, Bernier N, Sever V, Kowalczyk P, Bernard M, Cyrille M-C, Tran N-P, Hippert F and Noé P 2021 Improvement of phase-change memory performance by means of GeTe/Sb<sub>2</sub>Te<sub>3</sub> superlattices *Phys. Status Solidi RRL* **15** 2000538
- [66] Ding K, Wang J, Zhou Y, Tian H, Lu L, Mazzarello R, Jia C, Zhang W, Rao F and Ma E 2019 Phase-change heterostructure enables ultralow noise and drift for memory operation *Science* **366** 210–5
- [67] Shen J, Lv S, Chen X, Li T, Zhang S, Song Z and Zhu M 2019 Thermal barrier phase change memory *ACS Appl. Mater. Interfaces* **11** 5336–43
- [68] Gholipour B 2019 The promise of phase-change materials *Science* **366** 186–7
- [69] Wang X, Wu Y, Zhou Y, Deringer V L and Zhang W 2021 Bonding nature and optical contrast of TiTe<sub>2</sub>/Sb<sub>2</sub>Te<sub>3</sub> phase-change heterostructure *Mater. Sci. Semicond. Process.* **135** 106080
- [70] Wang X et al 2022 Unusual phase transitions in two-dimensional telluride heterostructures *Mater. Today* **54** 52–62
- [71] Ding K, Li T, Chen B and Rao F 2021 Reliable 2D phase transitions for low-noise and long-life memory programming *Front. Nanotechnol.* **3** 649560
- [72] Hatayama S, Yamamoto T, Mori S, Song Y-H and Sutou Y 2022 Understanding the origin of low-energy operation characteristics for Cr<sub>2</sub>Ge<sub>2</sub>Te<sub>6</sub> phase-change material: enhancement of thermal efficiency in the high-scaled memory device *ACS Appl. Mater. Interfaces* **14** 44604–13

- [73] Yang Z *et al* 2022 Designing conductive-bridge phase-change memory to enable ultralow programming power *Adv. Sci.* **9** 2103478
- [74] Morilla M C, Afonso C N, Petford-Long A K and Doole R C 1997 The role of oxygen content in the crystallization kinetics of (Sb<sub>0.9</sub>Ge<sub>0.10</sub>)O<sub>x</sub> films *Phil. Mag. A* **75** 791–802
- [75] Solis J, Morilla M C and Afonso C N 1998 Laser-induced structural relaxation and crystallization phenomena in the picosecond time scale in GeSbO thin films *J. Appl. Phys.* **84** 5543–6
- [76] Wu W, He Z, Chen S, Zhai J, Song S and Song Z 2017 Investigation on the crystallization properties and structure of oxygen-doped Ge<sub>8</sub>Sb<sub>92</sub> phase change thin films *J. Phys. D: Appl. Phys.* **50** 095602
- [77] Solis J, Afonso C N, Trull J F and Morilla M C 1994 Fast crystallization GeSb alloys for optical data storage *J. Appl. Phys.* **75** 7788–94
- [78] van Pieterse L, Lankhorst M H R, van Schijndel M, Kuiper A E T and Roosen J H J 2005 Phase-change recording materials with a growth-dominated crystallization mechanism: a materials overview *J. Appl. Phys.* **97** 083520
- [79] Zalden P, Bichara C, van Eijk J, Braun C, Bensch W and Wuttig M 2010 Atomic structure of amorphous and crystallized Ge<sub>15</sub>Sb<sub>85</sub> *J. Appl. Phys.* **107** 104312
- [80] Krusin-Elbaum L, Shakhvorostov D, Cabral C, Raoux S and Jordan-Sweet J L 2010 Irreversible altering of crystalline phase of phase-change Ge–Sb thin films *Appl. Phys. Lett.* **96** 121906
- [81] Mazzarello R, Caravati S, Angioletti-Uberti S, Bernasconi M and Parrinello M 2010 Signature of tetrahedral Ge in the Raman spectrum of amorphous phase-change materials *Phys. Rev. Lett.* **104** 085503
- [82] Andrikopoulos K S, Yannopoulos S N, Voyiatzis G A, Kolobov A V, Ribes M and Tominaga J 2006 Raman scattering study of the a-GeTe structure and possible mechanism for the amorphous to crystal transition *J. Phys.: Condens. Matter* **18** 965–79
- [83] Andrikopoulos K S, Yannopoulos S N, Kolobov A V, Fons P and Tominaga J 2007 Raman scattering study of GeTe and Ge<sub>2</sub>Sb<sub>2</sub>Te<sub>5</sub> phase-change materials *J. Phys. Chem. Solids* **68** 1074–8
- [84] Sosso G C, Caravati S, Mazzarello R and Bernasconi M 2011 Raman spectra of cubic and amorphous Ge<sub>2</sub>Sb<sub>2</sub>Te<sub>5</sub> from first principles *Phys. Rev. B* **83** 134201
- [85] Płońska M and Plewa J 2020 Crystallization of GeO<sub>2</sub>–Al<sub>2</sub>O<sub>3</sub>–Bi<sub>2</sub>O<sub>3</sub> glass *Crystals* **10** 522
- [86] Zhang Y, Feng J and Cai B 2010 Effects of nitrogen doping on the properties of Ge<sub>15</sub>Sb<sub>85</sub> phase-change thin film *Appl. Surf. Sci.* **256** 2223–7
- [87] Nolot E, Sabbione C, Pessoa W, Prazakova L and Navarro G 2021 Germanium, antimony, tellurium, their binary and ternary alloys and the impact of nitrogen: an x-ray photoelectron study *Appl. Surf. Sci.* **536** 147703
- [88] Tuma T, Pantazi A, Le Gallo M, Sebastian A and Eleftheriou E 2016 Stochastic phase-change neurons *Nat. Nanotechnol.* **11** 693–9
- [89] Noor N and Silva H 2020 *Phase Change Memory for Physical Unclonable Functions, Applications of Emerging Memory Technology* (Berlin: Springer) pp 59–91